



Article

# Wireless Remote-Monitoring Technology for Wind-Induced Galloping and Vibration of Transmission Lines

Peng Wang , Yuanchang Zhong , Yu Chen and Dalin Li

School of Electronic Engineering, Chongqing University, Chongqing 400044, China; 202211131261@stu.cqu.edu.cn (Y.C.); lidalin@stu.cqu.edu.cn (D.L.)

\* Correspondence: 20221101078g@stu.cqu.edu.cn (P.W.); zyc@cqu.edu.cn (Y.Z.)

**Abstract:** In order to achieve wireless remote monitoring of wind-induced vibrations in power-transmission lines based on MEMS sensors, it is necessary to devise a method for reconstructing the wind swing curve, enabling the device's real-time performance to promptly acquire, restore, and analyze data. Based on existing single-axis vibration-sensitive components, a measurement array using self-powered MEMS sensors and spacers has been designed. The Orthogonal Matching Pursuit (OMP) algorithm is selected to obtain displacement data collected by sensors installed on the transmission-line spacers. Leveraging the inherent sparsity of the data, a Gaussian white noise regularization matrix is chosen to establish the observation matrix. Through the algorithm, wind data curve reconstruction is achieved, enabling the reconstruction of large-span wind-induced vibration information without distortion. The experimental results demonstrate that when applying the orthogonal tracking algorithm in transmission-line curve reconstruction, sparsity is selected based on the sampling length, that is, the number of sensors installed on the spacers is determined by the span length; a portion of the observation values are selected to generate the observation matrix; and the wind galloping data curve of the transmission line is well restored.

**Keywords:** MEMS sensors; Orthogonal Matching Pursuit (OMP) algorithm; wind-induced galloping



**Citation:** Wang, P.; Zhong, Y.; Chen, Y.; Li, D. Wireless Remote-Monitoring Technology for Wind-Induced Galloping and Vibration of Transmission Lines. *Electronics* **2024**, *13*, 4630. <https://doi.org/10.3390/electronics13234630>

Academic Editor: Fabio Corti

Received: 21 September 2024

Revised: 14 November 2024

Accepted: 21 November 2024

Published: 24 November 2024



**Copyright:** © 2024 by the authors. Licensee MDPI, Basel, Switzerland. This article is an open access article distributed under the terms and conditions of the Creative Commons Attribution (CC BY) license (<https://creativecommons.org/licenses/by/4.0/>).

## 1. Introduction

In the electric power industry, ensuring the stability and reliability of transmission lines is crucial for preventing galloping phenomena induced by environmental factors such as strong winds and icing, which can compromise line integrity and result in significant economic losses [1–6]. To mitigate the risks associated with galloping, various monitoring and early-warning systems have been developed [7–9].

In the realm of transmission-line dynamics, various research efforts have been directed towards understanding and mitigating the phenomenon of galloping, a complex vibration issue that poses significant threats to the operational safety and efficiency of power grids. Han Jingshan and his colleagues [1] introduced an early-warning methodology for transmission-line galloping, leveraging a Genetic Algorithm–Back Propagation (GA-BP) neural network algorithm to predict and preempt potential hazards. Liu Xinyu et al. [2] further enhanced the precision of galloping probability forecasts through ensemble forecasting techniques, marking a significant stride in risk assessment.

Addressing the influence of tensioned insulator strings, Liu Zhuli et al. [3] provided valuable insights into the design of transmission lines, highlighting the need for robust considerations in structural configurations. Chen Zhongyuan and Shi Changming, in their respective studies [4,5], delved into the underlying causes of galloping and proposed a suite of preventive measures aimed at mitigating its adverse effects. Tang Yuanchun et al. [6] underscored the critical role of real-time data acquisition, employing distributed fiber-optic sensing technology to monitor galloping and lightning strikes with unprecedented accuracy.

Research endeavors have also focused on modeling the galloping behavior of ice-covered conductors, with Huang Shan et al. [7] presenting a detailed investigation of the

single-mode model. Meanwhile, Xiao Wu Kaiti Tursun and his team [8] emphasized the operational safety of transmission lines, contributing to a broader understanding of the system's resilience under adverse conditions. On the international front, contributions from de Villiers et al. [9] included the development of a real-time sag monitoring system, while Venkatasubramani [10] and Karthikeyan [11] explored the potential of wireless network monitoring for transmission-line parameters within the context of smart grids. Advancements in sensor design were achieved by Callis et al. [12] and Wang et al. [13], who introduced innovative solutions to enhance monitoring capabilities. Hui et al. [14] and Gao et al. [15] further refined algorithms, improving the diagnostic accuracy and anti-interference properties of monitoring systems.

Investigations into the wind vibration response of transmission-tower-line systems were conducted by He et al. [16] and Zhong et al. (assuming [17] as the correct reference due to missing [18]), providing deeper insights into the structural dynamics under wind loading. Additionally, Li et al. [19] and Liang et al. [20] explored the fatigue performance and stochastic dynamic characteristics of transmission lines, addressing long-term durability concerns.

Li et al. [21] analyzed rain-wind-induced cable vibrations, extending the scope of environmental factors impacting transmission-line stability. Zhou et al. [22] proposed a theoretical model for rain-wind-induced in-plane galloping, significantly advancing the understanding of transmission-line dynamics under combined environmental loads. Together, these studies illustrate a comprehensive research landscape dedicated to enhancing the reliability and safety of power-transmission infrastructures.

Recent research efforts in the domain of synchronized phasor measurement unit (PMU) optimization configuration for power systems have been dedicated to developing mathematical models and algorithms aimed at achieving complete network observability, while considering channel capacity limitations, communication infrastructure costs, and smart-grid deployment [23–25]. Although these studies have enhanced the predictive accuracy of transmission-line galloping through algorithms, such as the GA-BP neural network algorithm proposed by Han Jingshan et al. [1], the ensemble forecasting methods by Liu Xinyu et al. [2], and the single-mode model research on ice-covered conductor galloping by Huang Shan et al. [7], they have primarily focused on prediction methods and have not delved into how to map data from the physical environment to digital twin models. This paper aims to establish a comprehensive system based on transmission-line galloping, filling this research gap by employing a data-driven model to map the physical environment to digital twin models, thereby more comprehensively understanding and predicting the dynamic behavior of transmission lines under environmental loads [12,13].

Building on this foundation, this study introduces a wireless remote-monitoring technology for wind-induced galloping and vibration of transmission lines, which is essential for real-time monitoring and analysis of the dynamic behavior of transmission lines under the influence of wind. A method for reconstructing the wind swing curve has been designed to ensure the timeliness of data acquisition, restoration, and analysis. A novel measurement array integrating self-energy MEMS three-axis sensors with spacers has been developed, employing the Orthogonal Matching Pursuit (OMP) algorithm to retrieve the displacement data collected by sensors mounted on the transmission-line spacers. The algorithm leverages the sparsity of the data and utilizes a Gaussian white noise regularization matrix to construct the observation matrix, enabling the reconstruction of the wind swing data curve and facilitating the accurate capture of large-span wind-induced galloping information.

The experimental results indicate that when the Orthogonal Matching Pursuit (OMP) algorithm is applied to the reconstruction of the transmission-line curve, the sparsity level is selected based on the sampling length, meaning the number of sensors installed on the spacers is determined by the span length. By inputting the fundamental parameters into the algorithm, the wind galloping data curve can be successfully reconstructed. This technological advancement not only enhances the accuracy of transmission-line gallop-

ing monitoring but also provides real-time data support for digital twin models, further strengthening the understanding and predictive capabilities of the dynamic behavior of transmission lines under environmental loads.

## 2. Hardware Design of Spacer Bar + Sensor Array

### 2.1. Measurement Principle of MEMS Three-Axis Inertial Sensor

The sensor designed for this project operates on the principle of electromagnetic induction, eliminating the need for an external power supply. It effectively converts the velocity of a moving object into an electromotive force induced within the coil, outputting a signal in the form of an electrical current. A distinctive feature of this sensor is its self-powered nature, harnessing mechanical energy from the object under test and converting it into electrical energy, thereby reducing reliance on external power sources. The addition of an electromagnetic interference (EMI) shielding coating to the external casing of the sensor provides some protection against weather and electromagnetic interference. Additionally, the sensor boasts a broad operational bandwidth, offering flexible adaptability across various application scenarios.

Figure 1 illustrates the basic structural principle of the single-axis micro-inertial magnetoelectric velocity sensing element within the three-axis sensor. Its core components consist of stationary parts (frame, housing, protective cover), moving units (vibrating coil, diaphragm), and an elastic support system.

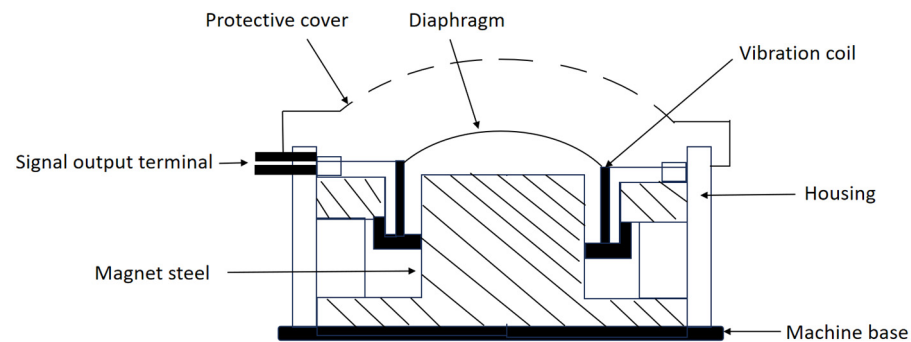


**Figure 1.** Schematic diagram of the basic structure and principle of a single-axis micro inertial magnetoelectric velocity measurement element.

As depicted in Figure 1, the constant magnetic flux structure with a moving coil as the sensitive element can effectively detect changes in the magnetic field, thus achieving high-precision measurements. According to Faraday's law of electromagnetic induction, when there is relative motion between the coil and the magnet, the electromotive force induced in the coil is given by

$$e = BDNv \quad (1)$$

where  $B$  is the magnetic flux density in the air gap,  $D$  is the circumference of each coil turn,  $N$  is the number of turns of the coil in the air gap magnetic field, also known as the effective number of turns, and  $v$  is the relative velocity between the coil and the magnet along the axis direction.

Once the sensor's structure is determined,  $B$ ,  $D$ , and  $N$  in the formula become constants, and the sensor's sensitivity  $S$  is

$$S = e/v \quad (2)$$

Thus, we obtain

$$S = BDN \quad (3)$$

In Formula (4),  $\vec{u}_s(t)$  denotes the induced electromotive force (EMF) in the coil,  $R_s$  signifies the coil's equivalent direct current (DC) resistance,  $L_s$  represents the coil's equivalent inductance, and  $\vec{U}_0(t)$  is the open-circuit output voltage of the device. When a moving-coil

magnetolectric sensor is interfaced with a subsequent measurement circuit, the input impedance of this circuit is designated as  $Z_i$ . The equivalent circuit is essential for the accurate assessment of the sensor's performance in transducing mechanical vibrations into electrical signals, which is particularly relevant in the field of precision measurement and monitoring within various engineering applications.

The output voltage of the equivalent circuit is derived from circuit principles as

$$\vec{U}_0 = \vec{U}_s \frac{1}{1 + \frac{R_s + R_L}{Z_i} - \omega^2 L_s C_c + j\omega[(R_s + R_L)C_c + \frac{L_s}{Z_i}]} \quad (4)$$

In the equation,  $\vec{U}_s$  denotes the induced electromotive force (EMF) of the generator coil;  $R_s$  represents the resistance of the coil;  $L_s$  signifies the inductance of the coil;  $C_c$  refers to the distributed capacitance of the transmission cable;  $R_c$  is the resistance of the transmission cable; and  $Z_i$  is the load impedance (input impedance of the amplifier), which corresponds to the input impedance of the subsequent measurement circuit. Within this system, the load impedance is approximately equal to the resistance of the transmission cable; both the resistance and the distributed capacitance of the transmission cable are considered negligible; and the coil's equivalent inductance is not taken into account. Consequently, when  $R_i \gg R_s$ , the input voltage of the amplifier,  $u_i$  is approximately equal to  $u_s$ .

Based on an in-depth analysis of the aforementioned principles, we conducted a comprehensive circuit design. In the signal amplification circuit, we selected OPA2836, an operational amplifier with an outstanding performance. This operational amplifier is characterized by low noise, low power consumption, high precision, and a wide operating voltage range between 2.5 V and 5.5 V, along with a bandwidth of 2.5 MHz. The overall system is powered by a single 3.6 V power supply, and at the non-inverting terminal, we specifically designed a bias voltage-supply mechanism of 1.8 V. This bias voltage is uniformly provided by a shared bias circuit. The shared bias circuit can ensure that all operational amplifiers receive the same magnitude and stable bias voltage at their non-inverting terminals, ensuring the stability and reliability of the system. By finely adjusting the amplification gain of the bias circuit, we are able to precisely condition the monitoring signals acquired by the vibration-sensitive elements to a range of  $1.8 \pm 1.5$  V. The specific implementation of this design process is illustrated in Figure 2.

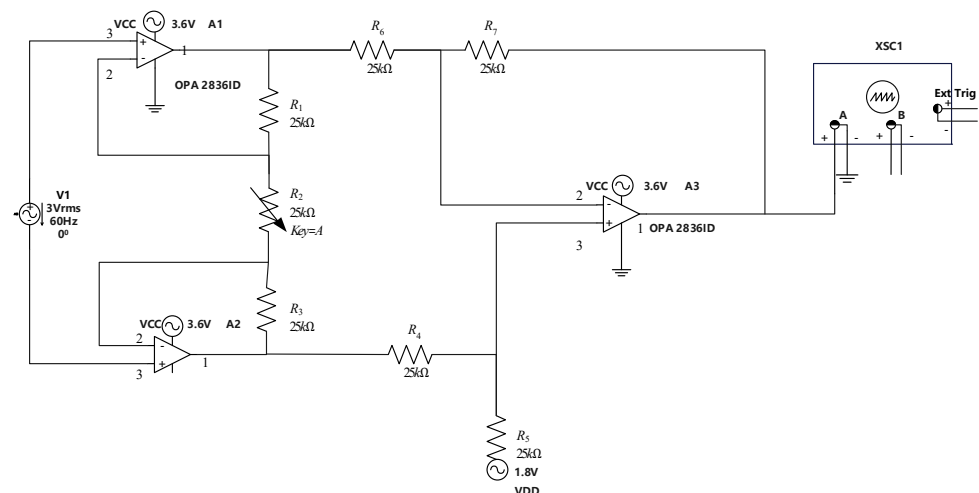


**Figure 2.** Schematic of the vibration signal amplification circuit.

Figure 2 illustrates the vibration signal-amplification circuit. In this figure, the operational amplifiers  $A_1$  and  $A_2$  serve as voltage followers, forming the differential pre-input stage of the sensitive element with a very high input impedance;  $A_3$  converts the differential input to a single-ended output. A and B: These are the input channels of the oscilloscope,

which can be connected to different points in the circuit to observe the voltage changes at these points.

The output voltage of the amplifier is known from electronic circuit theory as

$$u_o(t) = \left(1 + \frac{2R_5}{R_2}\right) \frac{R_7}{R_6} u_s(t) \quad (5)$$

From Equation (5), it can be seen that the voltage amplification factor of the amplifier, that is, the voltage gain, is

$$A_v = \frac{u_o(t)}{u_s(t)} = \left(1 + \frac{2R_5}{R_2}\right) \frac{R_7}{R_6} \quad (6)$$

By changing the value of  $R_2$ , the detection signal ranging from 0 to 3 V can be obtained.

Based on the single-axis micro-vibration sensor described above, a three-axis vibration sensor can be constructed by installing the designed single-axis vibration sensor along the X, Y, and Z axes to form a three-axis MEMS sensor. Subsequently, an intelligent chip is used to collect, store, and process the signals from the three-axis sensor to obtain the output voltage corresponding to the position coordinates of the first I spacer bar caused by wind-induced galloping:  $u_{ix}(t)$ ,  $u_{iy}(t)$ ,  $u_{iz}(t)$ . Finally, a WSN/GPRS/BD three-network fusion communication module is developed to achieve the remote transmission of signals.

Based on the aforementioned theory, and according to the spatiotemporal sparse characteristics of large-span transmission line wind-induced galloping, compressed sensing and the sparsity of data are used to reconstruct the complete power-line galloping signal, from which the wind-induced galloping curve of the power line under different wind loads can be derived.

## 2.2. Spacer Bar + Self-Powered MEMS Three-Axis Inertial Sensor Single Model

Through research on existing transmission line wind-induced galloping monitoring system designs, it is known that the selection of sensor installation positions on the transmission line is particularly important. To achieve non-uniform sampling and construct sparse signals, while reducing the cost of the device and facilitating subsequent maintenance and replacement, sensors are installed on the spacer bars of the transmission lines to meet the needs of health monitoring under extreme environmental conditions for large-span transmission lines. The physical model of the spacer bar + self-powered MEMS three-axis inertial sensor is shown in Figure 3.

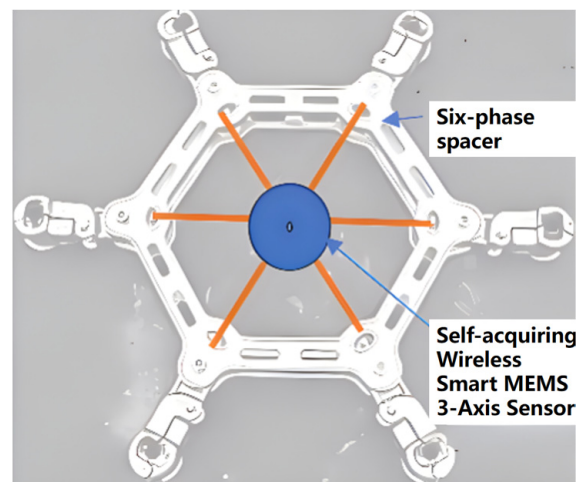


**Figure 3.** The physical model of the spacer bar + self-powered MEMS three-axis inertial sensor.

This single unit uses an insulating rod to fix the self-powered wireless intelligent MEMS three-axis sensor at the geometric center of the six-split spacer bar. At time  $t_0$ , the equilibrium position coordinates of the  $I$ -th spacer bar are  $I_{i0} (x_{i0}, y_{i0}, z_{i0})$ . Under the influence of environmental factors, at time  $t_1$ , after wind-induced galloping occurs, the position coordinates of this  $I$ -th spacer bar are  $I_{i1} (x_{i1}, y_{i1}, z_{i1})$ . By installing the MEMS inertial sensor in the center of the spacer bar, the change amount  $\Delta$  from  $t_0$  to  $t_1$  can be easily obtained.

Assuming that there are  $N$  spacer bars distributed in the large-span range, then  $N$  MEMS inertial sensors will obtain the wind-induced galloping change amounts at their respective different positions:  $\Delta_1, \Delta_2, \dots, \Delta_i, \Delta_N$ . When excessive or rapid changes in wind-induced oscillation are observed, it can be considered that the transmission line is about to experience or is already experiencing oscillation-induced faults. At this time, the system will issue a timely warning to achieve real-time monitoring of the transmission line. The general span between high-voltage line towers is 300 to 400 m. The minimum distance between dampers should not be less than 0.5 m, the average sub-span distance is 50 m to 60 m, and the end sub-span distance should be controlled between 25 m and 35 m. These regulations ensure the safety and stability of high-voltage power-transmission lines.

### 3. Establishment of the Wind Galloping Curve Model

#### Mechanical Analysis of the Galloping Model

A small section of the transmission line is taken as a wire element for force analysis and the force analysis diagram is drawn as shown in Figure 4.

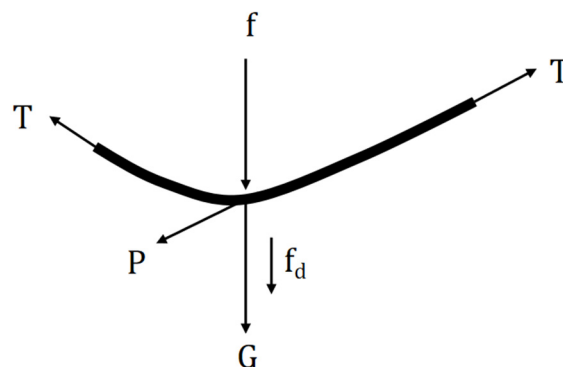


Figure 4. Force analysis diagram of the wire element.

$G$  is the self-weight of the wire, always pointing vertically downward;  $f$  is the air resistance, which is always opposite to the direction of the wire's movement;  $T$  is the tension of the wire, which exists along the tangential direction of the wire. Under the action of the wind, the tension  $T$  of the wire is dynamic. The wire deforms under the action of the tension, and its length becomes  $s$ . According to Hooke's law, we can obtain

$$s = \ell(1 + T/EA) \tag{7}$$

In Formula (7),  $\ell$  is the original length of the wire,  $E$  is the modulus of the wire,  $A$  is the cross-sectional area, and  $T$  is the tension the wire is subjected to. The wind acts on the wire in the form of wind pressure. When the wind blows the wire, the wire will vibrate, and the expression is as follows:

$$y = y_m \sin \frac{2\pi}{\lambda} x \sin \omega_j t \tag{8}$$

in which  $y$  represents the amplitude of the wire vibration (mm);  $y_m$  represents the maximum amplitude (mm);  $\lambda$  represents the wavelength of the wire vibration;  $F$  represents the frequency of the wire vibration;  $x$  represents the distance from the vibration point to the

end of the wire (m);  $t$  represents time (s); and  $f_d$  represents the alternating electrodynamic force between the wires, with a variation frequency of 2. By synthesizing the forces on the wire, a combined vibration force  $F$  is obtained, and the vibration frequency of the combined vibration force is set as  $f'$ . When the rate of change in the resistance is greater than the rate of change in the vibration force, the transmission line vibrates stably; when the rate of change in the resistance is less than the rate of change in the vibration force, the transmission line may exhibit galloping.

Due to the action of wind load, the wire will also deviate within the vertical plane and no longer lie in the vertical plane, so the vertical component of the tension is no longer 0. At this time, the expressions for each component of the tension on the wire are

$$\left. \begin{aligned} \frac{\partial}{\partial \ell} \left( \frac{T}{1+T/EA} \frac{\partial x}{\partial \ell} \right) &= 0 \\ \frac{\partial}{\partial \ell} \left( \frac{T}{1+T/EA} \frac{\partial y}{\partial \ell} \right) &= \rho g - F_y \\ \frac{\partial}{\partial \ell} \left( \frac{T}{1+T/EA} \frac{\partial z}{\partial \ell} \right) &= -F_z \\ \frac{\partial}{\partial \ell} \left( \frac{GI_p}{1+T/EA} \frac{\partial \theta}{\partial \ell} \right) &= M + F_M \end{aligned} \right\} \quad (9)$$

At the same time, the geometric constraint expression for the wire is

$$\left( \frac{\partial x}{\partial \ell} \right)^2 + \left( \frac{\partial y}{\partial \ell} \right)^2 + \left( \frac{\partial z}{\partial \ell} \right)^2 = (1 + T/EA)^2 \quad (10)$$

in which  $\ell$  is the original length of the wire;  $\rho$  is the unit length mass of the wire;  $GI_p$  is the torsional stiffness of the wire;  $M$  is the eccentric torque of the wire;  $T$  is the axial tension that the wire is subjected to;  $F_y$  and  $F_z$  represent the wind loads in the Y and Z directions that the wire is subjected to, respectively; and  $F_M$  is the torque the wire is subjected to.

Comprehensively considering the weight of the transmission wire, the drag force, lift force, and resistance of the wind on the wire, the tension of the wire, and the torque produced by the wire twisting, the dimensionless aerodynamic coefficient of the wire is used as the key parameter, including the lift coefficient  $C_L$ , the drag coefficient  $C_D$ , and the torsion coefficient  $C_M$ ; the expressions are as follows [21]:

$$C_L = \frac{F_L}{\rho U^2 L d / 2} \quad (11)$$

$$C_D = \frac{F_D}{\rho U^2 L d / 2} \quad (12)$$

$$C_M = \frac{M}{\rho U^2 l d^2 / 2} \quad (13)$$

in which  $\rho$  is the air density,  $U$  is the wind speed,  $L$  is the effective length of the wire model, and  $d$  is the wire diameter. During the motion of the wire, the angle of attack will change continuously, and the aerodynamic force on the wire will also change accordingly; the expression is as follows [21]:

$$[F_L \quad F_D \quad M]^T = \frac{1}{2} \rho U d [C_L(\alpha) \quad C_D(\alpha) \quad d C_M(\alpha)]^T \quad (14)$$

in which the change in the angle of attack is expressed as

$$\alpha \approx \theta - \left( \frac{R \theta_0 + V_0}{U} \right) \quad (15)$$

in which  $\theta$ ,  $R$ ,  $\theta_0$ , and  $V_0$  are the wire twist angle, characteristic radius (approximately half the wire radius), twist angular velocity, and vertical movement speed, respectively.

## 4. Reconstruction and Simulation Experiment of Wind Galloping Curve

### 4.1. Sparse Sensing Model

Traditional signal- or image-sampling methods follow the Shannon–Nyquist sampling theorem: the sampling rate must be at least twice the highest-frequency component present in the signal, which places high demands on the sampling instruments. However, the compressed sensing theory proposed in 2004 allows for the acquisition and representation of signals at rates significantly below the Nyquist rate by utilizing their inherent low-dimensional structure, enabling the reconstruction of signals from severely insufficient measurements. The process is illustrated in Figure 5.

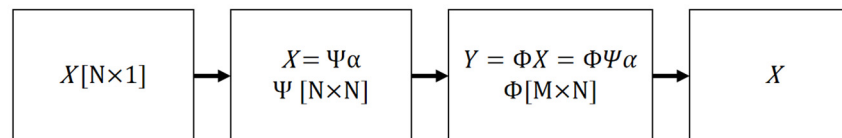


Figure 5. Theoretical framework of compressed sensing.

Assuming the signal  $Y$  is a one-dimensional real-valued signal with a finite length  $N$ . Regard it as a spatial  $N \times 1$  dimensional column vector, whose element values can be represented as  $X[n]$ , where  $n$  is a natural number less than  $N$ , and can be seen as a one-dimensional vector of length  $N$ . Since any signal can be represented as a linear combination of  $N \times 1$  dimensional basis vectors  $\{\phi_i\}_{i=1}^N$  (this basis is an orthonormal basis), the basis matrix  $\Psi = [\phi_1 | \phi_2 | \dots | \phi_N]$  is an  $N$ -dimensional sparse matrix with vectors  $\{\phi_i\}_{i=1}^N$  as its column vectors. Therefore, it can be expanded on this orthonormal basis as follows:

$$X = \sum_{i=1}^N \alpha_i \phi_i = \Psi \alpha. \quad (16)$$

The projection coefficients of the signal  $\alpha$  onto the basis matrix  $\Psi$ , despite  $\alpha$  containing numerous zeros, maintain the same dimensionality as the original dynamic signal, thus constituting a high-dimensional signal representation. This representation is indicative of the signal in the spectral domain, whereas the original signal is represented in the time domain. If the coefficients exhibit  $K$  ( $K \ll N$ ) non-zero elements with the rest being zero, the signal is termed  $K$ -sparse, with  $K$  denoting the degree of sparsity of the signal. Furthermore, if the coefficients consist predominantly of  $K$  significant values while the remaining values are minimal, the original signal can be approximated by these few substantial coefficients, thereby characterizing the signal as compressible.

Assuming a signal of length  $N$  has projection coefficients on the transform basis that are  $K$ -sparse, we design an observation matrix unrelated to the size of  $A$ , which is composed of  $M$   $N$ -dimensional column vectors. We project the sparse vibration waveform signal onto this sampling matrix to obtain the mapping of  $xx$  on this observation matrix, and finally obtain the  $M$ -dimensional measurement value  $Y$ , achieving data compression. Common types of observation matrices and their characteristics are as follows: the random Gaussian measurement matrix which has strong randomness, can easily meet the Restricted Isometry Property (RIP) condition, and requires fewer measurements for exact reconstruction; the random Bernoulli measurement matrix which also meets the RIP condition and is easier to store, but the coding process is more complex and cannot be directly generated by built-in functions of programming languages; the partial Hadamard measurement matrix which belongs to the orthogonal matrices and requires fewer measurements for exact reconstruction, but requires the dimension  $N$  to be a positive integer power of 2 or a multiple of 12 or 20; the partial Fourier orthogonal measurement matrix which has strict requirements for the value of sparsity; the random sparse measurement matrix which consists only of 0 and 1, and requires each column to have a specified number ( $d$ ) of 1s, and  $d < M$ , which is easy to construct and store in practical applications; and the Toeplitz



matrix and circulant measurement matrix—the circulant measurement matrix is a special form of Toeplitz matrix, both are generated by randomly generating a column vector, then cyclically shifting the column vector, and finally normalizing the column vector to generate the measurement matrix, which is easy to implement in hardware applications. The mathematical expression for this process is

$$Y = \Phi X = \Phi \Psi \alpha = \Theta \alpha \quad (17)$$

where  $Y$  is an  $M \times 1$  vector, which is the observation value of  $X$ ;  $\Theta = \Phi \Psi$  is an  $M \times N$  matrix, also known as the sensing matrix, composed of the sampling matrix and the sparse basis. The sampling matrix and the sparse matrix must be independent of each other, that is, their rows and columns cannot represent each other, and they must satisfy the matrix's Restricted Isometry Property (RIP). Although  $M \ll N$ , the reconstruction process is an NP-HARD problem, and the  $N$ -dimensional original signal  $X$  cannot be directly solved using the  $M$ -dimensional measurement value. However, considering that  $\alpha$  is  $K$ -sparse and  $K < M \ll N$ , the original signal in the sparse domain can be approximated by solving an optimization problem, and finally, the recovery value of the original signal can be obtained through the inverse transformation of the sparse matrix. In summary, the original objective function can be approximated and equivalent to

$$\begin{cases} Y = \Phi X = \Theta \alpha \\ \alpha^{(1)} = \arg \min_{\alpha \in R^N} \|\alpha\|_1 \end{cases} \quad (18)$$

Considering the large-span wind-induced vibration monitoring approach of this project, which primarily relies on the placement of monitoring nodes on spacer dampers, the monitoring sampling signals themselves exhibit sparsity. This sparsity can be leveraged using compressed sensing methods to combine the existing data acquisition process with the reconstruction process, fully utilizing the sparse nature of the data to reconstruct the complete signal. For this project, we have selected one of the compressed sensing algorithms, Orthogonal Matching Pursuit (OMP), to reconstruct the data. The Orthogonal Matching Pursuit (OMP) algorithm is an improvement over the Matching Pursuit (MP) algorithm. The OMP algorithm is a type of greedy iterative algorithm with the same basic principle as MP, which involves selecting, in each iteration, the column that has the maximum correlation with the current residual vector. Subsequently, the related part is excluded from the observation vector, and the iteration is repeated. In each iteration, the column that is most correlated with the residual is identified to minimize the least squares error, and this column is subtracted from the data vector. The residual is then subjected to further iterations until the correct vector is ultimately determined. The flowchart for the reconstruction process of the vibration curve based on the OMP algorithm is shown in the table below (Algorithm 1).

In this project, to address the implementability of matrix hardware, the conductor is divided into  $N$  nodes using spacer dampers as boundaries, with  $M$  sensors installed on the spacer dampers, and a measurement matrix is designed accordingly. The rows of this matrix correspond to the sensors, and the columns correspond to the positions of the spacer dampers. The number of iterations is set to  $K$ , and the exploration obtained from each iteration is assessed to prevent data overfitting.

**Algorithm 1:** Image reconstruction from incomplete data

Input: Incomplete data set  $D$  with missing values.

Output: Reconstructed image  $I$  from the incomplete data set.

**Step 1:** Initialization

Begin by initializing the iteration counter  $K = 0$ .

**Step 2:** Data Loss Detection and Sampling

Detect the missing data in the input data set  $D$ .

Perform data loss detection sampling to identify the locations and extent of data loss.

**Step 3:** Design Measurement Matrix

Construct a measurement matrix  $M$  based on the detected data loss. This matrix will be used to guide the reconstruction process.

**Step 4:** CMP Reconstruction Algorithm

Apply the CMP (Compressed Sensing or Compressed Measurement Protocol)

reconstruction algorithm to the incomplete data set  $D$  using the measurement matrix  $M$ . This step involves iterative processing to estimate the missing data.

**Step 5:** Iteration Check

Determine if the number of iterations  $K$  is satisfied with the predefined stopping criteria. These criteria may include a maximum number of iterations, a convergence threshold, or a minimum improvement in the reconstruction quality.

If the stopping criteria are not met, set  $K = K + 1$  and return to Step 4.

If the stopping criteria are met, proceed to the next step.

**Step 6:** Image Reconstruction

Use the output from the CMP reconstruction algorithm to reconstruct the image  $I$ . This step involves assembling the estimated data to form a complete image.

**Step 7:** Termination

The algorithm terminates, and the reconstructed image  $I$  is output.

**4.2. OMP Algorithm Verification and Result Analysis**

For the convenience of simulation, only the vibration in the vertical direction of the transmission line is considered during sampling. Let  $X$  represent the vector set of the vertical amplitudes collected by the sensors on each spacer bar. When the galloping reaches a stable state, the relationship with the maximum amplitude  $A_0$ , span  $L$ , galloping half-wavelength  $n$  ( $n = 1, 2, 3$ ), position of the galloping on the wire  $i$ , galloping frequency  $f$ , and time  $t$  can be represented by Formula (19).

$$X_i = A_0 \sin\left(\frac{n\pi}{L}i\right) \sin(2\pi ft) \quad (19)$$

Taking the galloping event on 3 January 2018, at the N7791–N7792 section of the 1000 kV Changji–Guquan ultra-high-voltage DC transmission line as an example [22], the span of the galloping event was 399 m, the amplitude was 2–3 m, and the vibration frequency was about 0.6 Hz. Substituting into the formula gives

$$X_i = 3 \sin\left(\frac{3\pi}{399}i\right) \sin(3.768t) \quad (20)$$

Considering that there will be various other factors interfering when the actual galloping occurs, some additional trigonometric functions are added as interference factors,  $x_1, x_2, x_3, x_4$ , as shown in Table 1, to obtain the final signal used,  $X$ .

Considering that the sensors in this project need to be suspended from the spacer bars, and the spacer bars need to be installed non-uniformly when mounted on the transmission line, the sparsity level  $K$  is selected to represent the number of spacer bars when establishing the transmission-line galloping curve reconstruction system. When generating observation signals,  $K$  indices are randomly generated, and the parts other than the indices are set to zero.

**Table 1.** Interference functions and intervals table.

Interference Function	Interference Interval
$x_1 = 0.6 \sin(\frac{2\pi i}{100}) \sin(3.768t)$	$1 < i < 75$
$x_2 = 0.6 \sin(\frac{2\pi i}{256}) \sin(3.768t)$	$142 < i < 200$
$x_3 = 0.4 \sin(\frac{2\pi i}{100}) \sin(3.768t)$	$284 < i < 310$
$x_4 = -0.4 \sin(\frac{2\pi i}{256}) \sin(3.768t)$	$338 < i < 440$

The observation matrix in the system uses a Gaussian white noise regularization matrix, which has good mathematical properties, is easy to analyze and process, and can provide more stable observation data. To verify the reliability of the wind galloping curve reconstruction method based on one of the compressed sensing algorithms, Orthogonal Matching Pursuit (OMP), while keeping the sparsity level  $K$  constant (set to 20), the number of observations  $M$  is taken as 40, 60, 70, 80, 96, 100, 120, and 140, and the time  $t$  is taken as 0.5 s, 1 s, 1.5 s, and 2 s for data simulation, with 50 repetitions for each set. The mean square error (MSE) and signal-to-noise ratio (SNR) are used as indicators of the reliability of the reconstructed signal, with their expressions as follows:

$$MSE = \frac{1}{m} \sum_{i=1}^m (x_i - \hat{x}_i)^2 \tag{21}$$

$$SNR = 10 \times \ln\left(\frac{\sum_{i=1}^m (x_i - \bar{x})^2}{MSE}\right) \tag{22}$$

where  $\bar{x}$  represents the mean of the signal  $X$ . The smaller the MSE and the larger the SNR, the closer the reconstructed signal is to the original signal, indicating higher reliability. Fifty simulation experiments were conducted, recording the MSE and SNR for each experiment and calculating the average values of the experimental errors and SNR, as shown in Table 2.

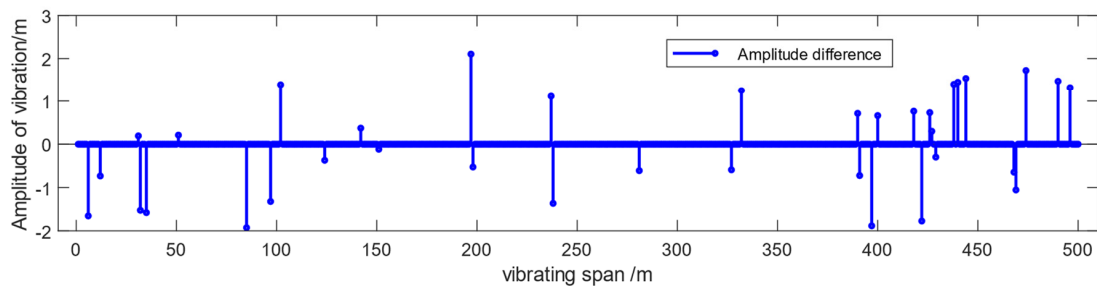
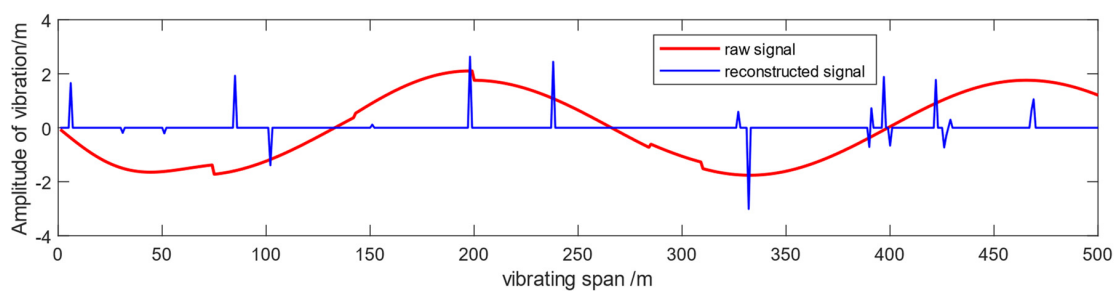
**Table 2.** Simulation results.

Observation count (M)	Proportion of observation (M/N)	Sparse point proportion (K/N)	MSE			
			t = 0.5 s	t = 1 s	t = 1.5 s	t = 2 s
40	8.0%	4.0%	0.327	0.121	0.130	0.324
60	12.0%		0.280	0.102	0.099	0.242
70	14.0%		0.194	0.069	0.073	0.177
80	16.0%		0.063	0.023	0.035	0.048
100	20.0%		0.015	0.007	0.004	0.015
120	24.0%		$3.62 \times 10^{-3}$	$5.341 \times 10^{-5}$	$1.814 \times 10^{-5}$	$4.715 \times 10^{-5}$
140	28.0%		$2.008 \times 10^{-6}$	$3.708 \times 10^{-7}$	$4.448 \times 10^{-6}$	$5.302 \times 10^{-7}$
Observation count (M)	Proportion of observation (M/N)	Sparse point proportion (K/N)	SNR			
			t = 0.5 s	t = 1 s	t = 1.5 s	t = 2 s
40	8.0%	4.0%	-2.4737	-2.4815	-2.7553	-2.4715
60	12.0%		-1.0083	-1.1602	0.3057	0.6757
70	14.0%		13.1784	11.884	19.7898	15.1464
80	16.0%		81.7881	42.6885	55.2846	97.0938
100	20.0%		176.1729	164.3679	126.4609	177.555
120	24.0%		246.0435	259.4576	251.6442	251.7981
140	28.0%		303.9248	288.263	287.8069	270.3841

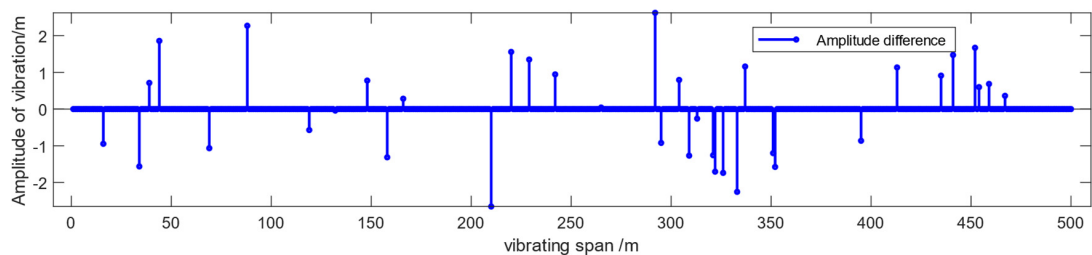
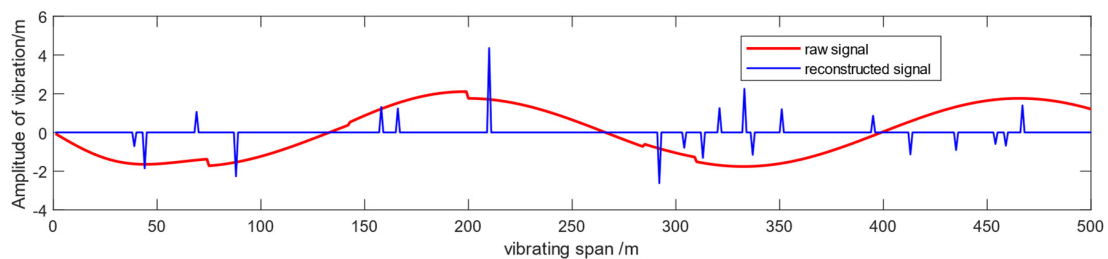
It has been observed that the root mean square error (RMSE) decreases with an increase in the number of observation values, regardless of the time elapsed, as long as the sparsity remains constant. When the vibration time is moderate ( $t = 1$  s or  $1.5$  s), even with a smaller number of observation values, the reconstruction effect is quite remarkable, with the error being only around 0.125. When  $t$  is too long or too short, that is, when the vibration frequency of the galloping curve is too low or too high, the reconstruction effect is relatively poor if the number of observation values is low. However, the overall error remains below

0.35, and the error can rapidly decrease when the number of observation values increases from 40 to 80. When the number of observation values exceeds 70, the error can be reduced below 0.125, ensuring that the accuracy is still guaranteed.

According to the formula for the signal-to-noise ratio (SNR), signal reconstruction can be considered successful when the SNR is positive. The higher the average SNR obtained from the simulation experiment, the higher the probability of successful signal reconstruction. Regardless of the time elapsed, the SNR increases with an increase in the number of observation values. Figure 6, which shows the comparison of reconstructed and original signals and the amplitude difference diagram at  $t = 1$  s for different observation quantities, indicates that within the range in which the number of observation values is greater than 60 and less than 120, the SNR increases rapidly. This suggests that the precision of signal reconstruction significantly improves when the number of observation values is within the range of 60 to 120. After the number of observation values exceeds 120, the probability of successful signal reconstruction remains essentially constant.

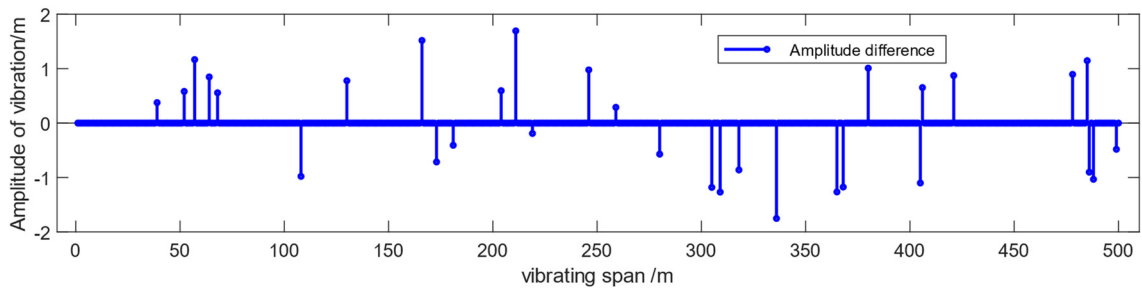
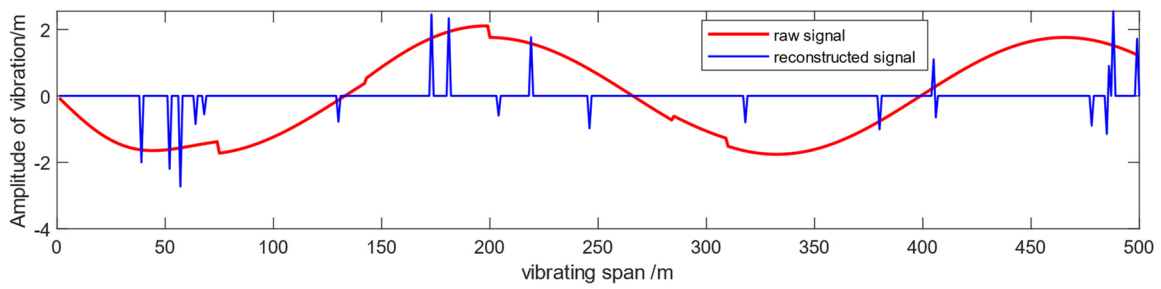


(a) The observed value is 40.

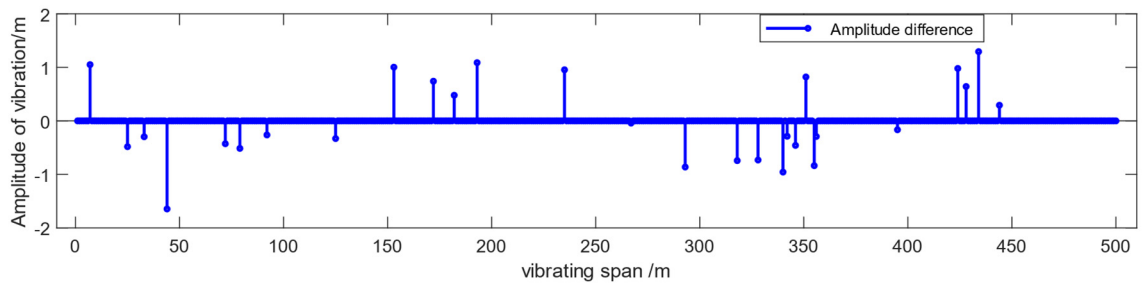
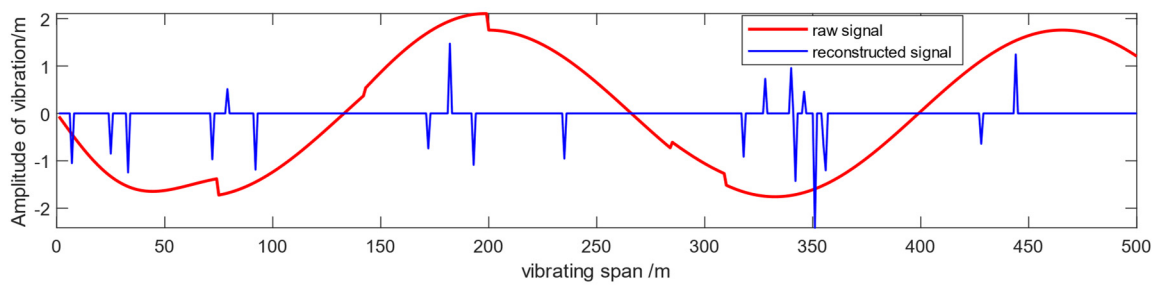


(b) The observed value is 60.

Figure 6. Cont.

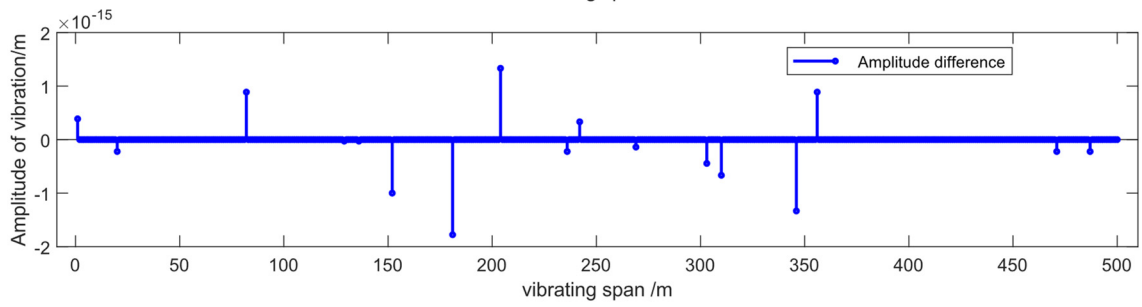
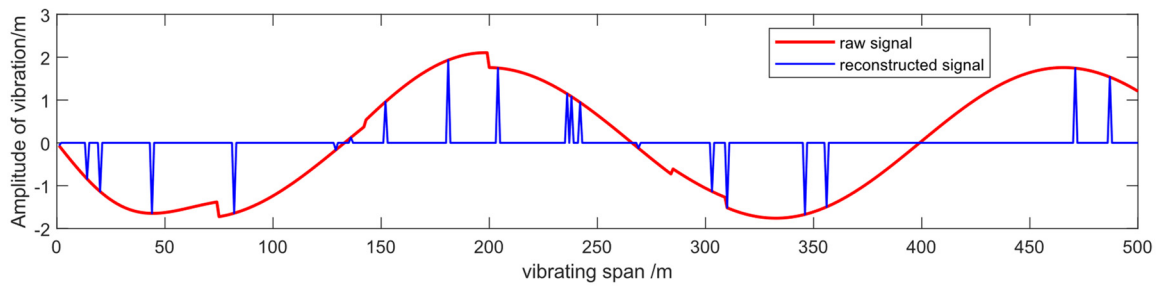


(c) The observed value is 70.

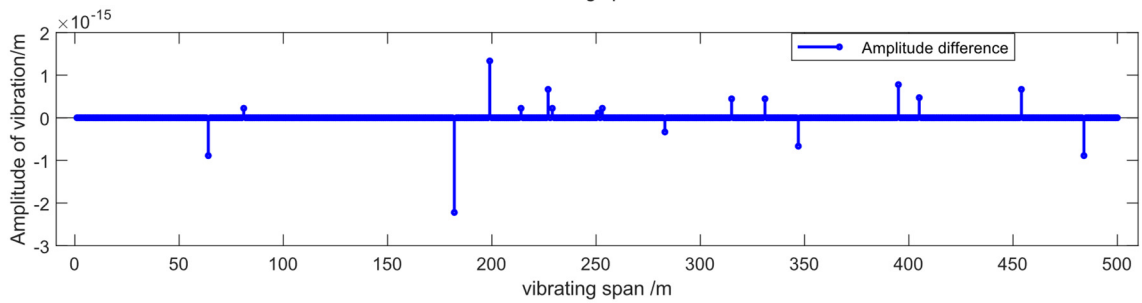
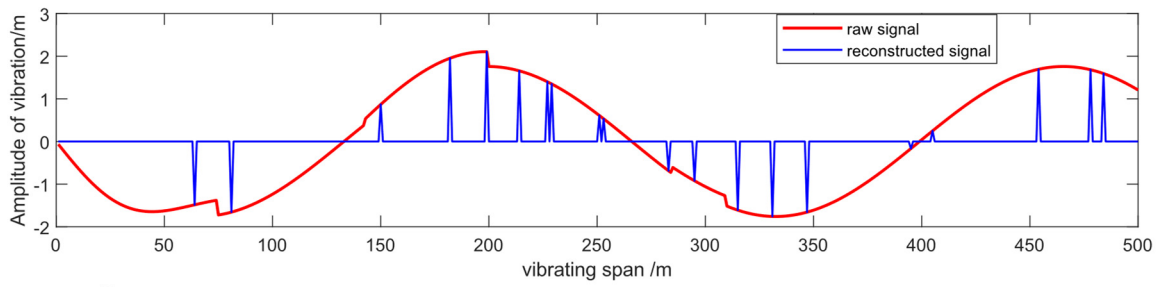


(d) The observed value is 80.

Figure 6. Cont.

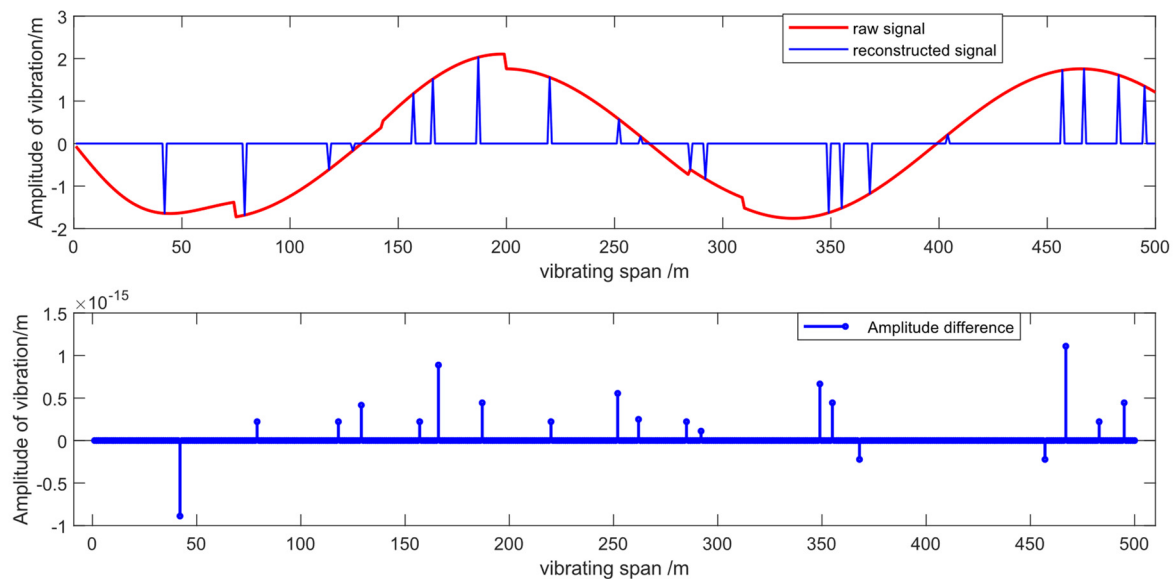


(e) The observed value is 100.



(f) The observed value is 120.

Figure 6. Cont.



(g) The observed value is 140.

**Figure 6.** Comparison graph and amplitude difference of reconstructed signal and original signal at different observation counts at  $t = 1$  s.

## 5. Conclusions

In this paper, a remote real-time monitoring system is proposed for the surveillance and analysis of galloping phenomena in overhead transmission lines under the influence of wind, with the aim of preventing electrical accidents. The system utilizes MEMS sensors to collect the displacement and acceleration data of the conductors and employs the Orthogonal Matching Pursuit (OMP) algorithm to process these data and reconstruct the wind-induced galloping curves. The study commences with a force analysis on the unit length of the transmission line to establish a mathematical model of wind-induced galloping. Subsequently, simulation experiments are conducted to verify the reliability and accuracy of the OMP algorithm under various observational conditions, ensuring that the reconstructed galloping curves have an error margin below 0.125. This provides an effective monitoring method for the safe operation of transmission lines.

**Author Contributions:** Conceptualization, P.W. and Y.Z.; Software, P.W. and Y.C.; Validation, P.W. and D.L.; Investigation, P.W.; Data curation, P.W.; Supervision, Y.Z. All authors have read and agreed to the published version of the manuscript.

**Funding:** This research was funded by the National Natural Science Foundation of China, U22B2095.

**Data Availability Statement:** Data are contained within the article.

**Conflicts of Interest:** The authors declare no conflicts of interest.

## References

1. Han, J.; Lv, H.; Li, D.; Li, Z.; Li, J.; Deng, Y. Transmission Line Galloping Early Warning Method Based on GA-BP Neural Network Algorithm. *Power Grid Clean Energy* **2021**, *37*, 1–7+14.
2. Liu, X.; Guo, Z.; Wang, C.; Wang, J.; Meng, G. Transmission Line Galloping Probability Prediction Method Based on Ensemble Forecasting. *Manuf. Autom.* **2023**, *45*, 175–179.
3. Liu, Z.; Huo, X.; Wu, C.; Wang, J.; Zhang, B.; Liu, G. Study on the Galloping Characteristics of Eight-Split Transmission Line Considering the Tension Insulator String. *J. Appl. Mech.* **2023**, *40*, 1085–1095.
4. Chen, Z.; Cui, Y.; Tang, Y.; Zhu, Y.; Dong, J. Analysis of the Causes of Transmission Line Galloping and Countermeasures. *Electron. Technol.* **2023**, *52*, 382–383.
5. Shi, C.; Dang, L.; Tang, Y.; Tong, M.; Tang, Y. Analysis of the Causes of Iced Galloping and Prevention Measures for Transmission Lines. *Integr. Circuit Appl.* **2023**, *40*, 364–365.

6. Tang, Y.; Li, C.; Huang, N.; Ding, C.; Zhang, Y. Progress in Monitoring Technology for Galloping and Lightning Strike of Overhead Transmission Lines Based on Distributed Fiber Optic Sensing. *Opto-Electron. Technol.* **2023**, *43*, 337–346.
7. Huang, S.; Liu, X.; Wu, H.; Wu, C.; Ye, Z. Comparative Study on Segmented Sparse Identification of Single-Mode Model for Iced Conductor Galloping in Stochastic Wind Field. *Mech. Q.* **2024**, *45*, 259–273.
8. Xiao, W.; Kaiti, T.; Zi Biremmu, A.; Mei, J. Research on Safety Analysis and Risk Prevention of Transmission Line Operation. *Light. Illum.* **2023**, *11*, 189–191.
9. de Villiers, W.; Cloete, J.H.; Wedepohl, L.M.; Burger, A. Real-time sag monitoring system for high-voltage overhead transmission lines based on power-line carrier signal behavior. *IEEE Trans. Power Deliv.* **2008**, *23*, 389–395. [[CrossRef](#)]
10. Venkatasubramani, K.; Karthikeyan, R. Monitoring of transmission line parameters using wireless networks in smart grid. In Proceedings of the 2014 International Conference on Intelligent Computing Applications (ICICA 2014), Coimbatore, India, 6–7 March 2014; pp. 330–334.
11. Liu, Y.J.; Yin, H.Y.; Wu, T. Transmission Line on-line Monitoring System Based on Ethernet and McWiLL. In Proceedings of the International Conference on Logistics, Engineering, Management and Computer Science (LEMCS 2015), Shenyang, China, 29–31 July 2015; pp. 680–683.
12. Callis, R.W.; Lohr, J.; Gorelov, I.A.; Kajiwaru, K.; Ponce, D.; Doane, J.L.; Tooker, J.F. An in-line power monitor for HE11 low loss transmission lines. In Proceedings of the Conference Digest of the 2004 Joint 29th International Conference on Infrared and Millimeter Waves and 12th International Conference on Terahertz Electronics, Karlsruhe, Germany, 27 September–1 October 2004; pp. 719–720.
13. Wang, Y.; Xiao, Y.; Zhao, X.F.; Wen, D.Z. Fabrication and Characterization of Monolithic Integrated Three-Axis Acceleration/Pressure/Magnetic Field Sensors. *Micromachines* **2024**, *15*, 412. [[CrossRef](#)]
14. Hui, Y.C.; Zhang, Y.C.; Tang, J.; Li, Z.; Chen, R.L.; Cui, Y.H. Clustering-based regularized orthogonal matching pursuit algorithm for rolling element bearing fault diagnosis. *Trans. Inst. Meas. Control* **2024**, *46*, 2795–2803. [[CrossRef](#)]
15. Gao, M.; Zhang, Y.; Yu, Y.; Lv, D.; Xi, R.; Li, W.; Gu, L.; Wang, Z. An Improved OMP Algorithm for Enhancing the Anti-Interference Performance of Array Antennas. *Sensors* **2024**, *24*, 2291. [[CrossRef](#)]
16. He, J.; Niu, J.; Li, L.; Liu, Z.; Liu, H.; Huang, Y.; Zhang, X.; Wang, E.; Luo, M. The Phase-to-Ground Fault Locating Method for the Wind Farm Transmission Line With the Single End Transient Information. *IEEE Access* **2024**, *12*, 115286–115295. [[CrossRef](#)]
17. Wang, X.; Yang, C.; Zhang, J.; Zhou, J.; Liang, H.; Jiang, J.; Cai, Y.; Huang, M.; Lan, Z. Study on the Wind Deviation Characteristics of Y-Type Insulator String under the Action of Strong Wind. *Adv. Civ. Eng.* **2024**, *2024*, 5542173. [[CrossRef](#)]
18. Zhong, Y.L.; Liu, Y.C.; Li, S.; Yan, Z.T.; Liu, X.P. Study on Wind Vibration Response and Coupling Effect of Transmission Tower-Line System Under Downburst. *IEEE Access* **2024**, *12*, 100120–100133. [[CrossRef](#)]
19. Li, Z.F.; Zhang, J.W.; Wang, H.N.; Bao, Y.J. Fatigue performance of power transmission tower system based on wind vibration fatigue. *Int. J. Power Energy Syst.* **2024**, *44*. [[CrossRef](#)]
20. Liang, Y.M.; Guo, Y.F.; Lin, Z.F. Using reservoir computing to solve FPK equations for stochastic dynamical systems under Gaussian or Non-Gaussian excitation. *Math. Comput. Simul.* **2024**, *226*, 645–662. [[CrossRef](#)]
21. Li, Y.L.; Xu, Y.L.; Xiang, H.Y.; Chen, B.; Shum, K.M.; Liao, H.L. Analysis of Rain-wind Induced Cable Vibration using Spatially Measured Aerodynamic Coefficients. *Adv. Struct. Eng.* **2014**, *17*, 961–977. [[CrossRef](#)]
22. Zhou, C.; Liu, Y.B. A theoretical model of rain-wind-induced in-plane galloping on overhead transmission tower-lines system. *Adv. Mech. Eng.* **2015**, *7*, 1687814015604590. [[CrossRef](#)]
23. Theodorakatos, N.P.; Babu, R.; Theodoridis, C.A.; Moschoudis, A.P. Mathematical Models for the Single-Channel and Multi-Channel PMU Allocation Problem and Their Solution Algorithms. *Algorithms* **2024**, *17*, 191. [[CrossRef](#)]
24. Singh, S.P.; Singh, S.P. Optimal cost wide area measurement system incorporating communication infrastructure. *IET Gener. Transm. Distrib.* **2017**, *11*, 2814–2821. [[CrossRef](#)]
25. Theodorakatos, N.P.; Babu, R.; Moschoudis, A.P. The Branch-and-Bound Algorithm in Optimizing Mathematical Programming Models to Achieve Power Grid Observability. *Axioms* **2023**, *12*, 1040. [[CrossRef](#)]

**Disclaimer/Publisher’s Note:** The statements, opinions and data contained in all publications are solely those of the individual author(s) and contributor(s) and not of MDPI and/or the editor(s). MDPI and/or the editor(s) disclaim responsibility for any injury to people or property resulting from any ideas, methods, instructions or products referred to in the content.